

**Slow release of fossil carbon during the Palaeocene-Eocene Thermal Maximum**

Ying Cui, Lee R. Kump, Andy J. Ridgwell, Adam J. Charles, Christopher K. Junium, Aaron F. Diefendorf,  
Katherine H. Freeman, Nathan M. Urban, Ian C. Harding

**This PDF file includes:**

Materials

Age model uncertainties

Additional model results

Model-data comparison

Sensitivity analysis

Figures S1 to S15

Tables S1 to S6

References

## 1. Materials

The core BH9-05 was collected by Store Norske Spitsbergen Kulkompani in 2005 and provided to the co-authors and collaborators under the auspices of the Worldwide Universities Network's pACE program (paleo-Arctic Climates and Environments; <http://wun.ac.uk/pACE>). Approximately 550 m of continuous drill core spanning the latest Paleocene and the earliest Eocene were recovered. The core BH9-05 includes the following Formations in stratigraphic order: 1) Grumantbyen Formation (highly bioturbated sandstones of offshore sand bars); 2) Frysjaodden Formation (continuous mud-stone dominated succession with sand-rich turbidite intervals and ash layers)<sup>1</sup>. The lowermost part of the core is characterized by Grumantbyen Formation sandstone, gradually transiting into Frysjaodden Formation dark gray shale. Lamination develops from 532 to 500 mbs of Frysjaodden Formation with abundant pyrite<sup>2</sup>. The lower part of the middle Frysjaodden Formation (500 to 409 mbs) is composed of coarser-grained greyish black shale characterized by thin bioturbated silt layers. For the purpose of this study sampling specifically avoided sandstone.

## 2. Age model uncertainties

Owing to the different age models for the duration of the PETM CIE<sup>3,4</sup> two cyclostratigraphic age model options were proposed for core BH9/05<sup>5</sup>. This study employs Option A of Charles *et al.* (ref. 4), where the Log Fe record from BH9/05 was tuned to the same parameter from ODP Site 1263 (the age model of ref. 2). The rate of carbon injection inferred in this study is thus dependent upon the BH9/05 age model proposed by Charles *et al.* (ref. 4). The use of the CIE as an external constraint on the age model was discussed by Charles *et al.* (ref. 4), who also demonstrated that there was no pronounced rise in sedimentation rates during the PETM. Here, we discuss further potential uncertainties associated with the BH9/05 age model, based on the following questions:

## 2.1. Is the PETM stratigraphically complete in core BH9/05?

Owing to the proximal depositional setting of our study material, we explore the possibility that unconformities may be present within the PETM CIE of core BH9/05.

The onset of the CIE is marked by a pronounced negative shift in  $\delta^{13}\text{C}$  values on a global scale (*e.g.* ref. 6). Thus any unconformities within this interval should be manifested as steps in the  $\delta^{13}\text{C}$  curve. For example, such steps are observed in the deep water records of the Walvis Ridge PETM owing to carbonate dissolution at the onset of the CIE (*e.g.* refs. 7,8). In Spitsbergen, we have recorded multiple transitional values to the most negative  $\delta^{13}\text{C}_{\text{TOC}}$  values after the onset of the CIE in core BH9/05. This suggests that if unconformities are present within the CIE onset, they are stratigraphically restricted to intervals below the resolution of the  $\delta^{13}\text{C}_{\text{TOC}}$  record, i.e. <30 cm. At the present time, we have no way of testing for the presence of such small-scale unconformities, but would note that such phenomena would lengthen the duration of the CIE onset, therefore lowering carbon injection rates further. The presence/absence of such unconformities within this interval would thus not alter our conclusion of low emission rates of carbon during the PETM onset.

Within the ‘core’ of the PETM CIE in BH9/05 there is a notable transition to darker laminated mudstones with elevated concentrations of pyrite (Figure 5 in ref. 2). Harding *et al.*<sup>9</sup> inferred the development of water column stratification during the core of the PETM CIE in Spitsbergen, which together with sea level rise and the warmer waters during the PETM resulted in anoxic conditions within the sediment. A decline in diversity is also observed in agglutinated foraminiferal assemblages in core BH9/05, consistent with low bottom water oxygen (J. Nagy pers. comm. 2011). Thus, rather than the erosive tractional currents required to generate unconformities on a scale that could bias cycle interpretations, the site of deposition demonstrates evidence for low bottom water oxygen conditions and thus low bottom water current velocities (a non-depositional hiatus is extremely unlikely in this foreland basin setting).

Conversely, through the recovery interval of the BH9/05 PETM CIE, there are indicators of anoxia within the sediment decline. We cannot therefore rule out the possibility of small-scale unconformities being present within this interval, although no sedimentological indicators support such a contention.

## **2.2. Were the time-series altered by short-lived changes in sedimentation rate, or overprinting from a non-orbital influence?**

Comparison of Fe/Mn records from core BH9/05 with wt. % TOC time-series records from an additional PETM locality (the Longyearbyen section of ref. 9) has illustrated that the same cycles are present at both sites, indicating the cycles in the time-series are not result of stochastic noise or site-specific processes<sup>5</sup>. However, Charles *et al.*<sup>5</sup> noted the presence of three additional cycles within the PETM interval, compared to the Röhl *et al.*<sup>3</sup> age model. If these cycles are interpreted as precession cycles, then the duration of the PETM is consistent with that proposed by Murphy *et al.*<sup>4</sup>.

Here we must explore the possibility that rapid changes in sedimentation rate, or non-orbital influences altered the time-series records, producing additional cycles. Charles *et al.*<sup>5</sup> noted that cycles with frequencies from 4-6 m were present in the Fe/Mn time-series records from core BH9/05, and interpreted these cycles as precession cycles. Analysis of the time-series illustrates that ~5 m cycles are predominant in the interval from 530.42-498.95 m, whereas ~4 m cycles predominate in the interval 498.95-485.75 m, as illustrated in the wavelet spectra from these records (Figure 4 in ref. 5). Thus the range of cycle frequencies for the inferred precession cycles (excluding those marked with an asterisk) can be explained by a small change in sedimentation rate at ~500 m, with more condensed sedimentation in recovery phase II of the PETM. The consistent cycle thickness within these two respective intervals is consistent with quasi-periodic changes in insolation associated with orbital forcing (excluding the cycles marked with an asterisk). Recent age models constraining the duration of the CIE<sup>3, 4</sup> suggest the 4-6 m and 20 m cycles

are derived from precession and eccentricity forcing respectively, consistent with the cycle ratio observed between these two components<sup>5</sup>.

Conversely, the three ~2 m low amplitude cycles marked with an asterisk are stratigraphically thinner than the 4-6 m cycles discussed above. The difference in cycle thickness may suggest these three cycles have a different derivation, such as non-orbital influences on the time-series. Alternatively, intervals of relatively condensed sedimentation could also result in precession cycles with a reduced stratigraphic thickness. The ambiguous origin of these cycles therefore substantiates the need for two different cyclostratigraphic age options<sup>5</sup>, to account for this uncertainty. Here we utilise Option A, which excludes the three cycles marked with an asterisk. It should be noted that by employing Option B (containing the three additional cycles, consistent with the Murphy *et al.*<sup>4</sup> age model) a slower rate of carbon injection than that inferred in this study would be generated, and therefore the use of Option B would not alter our conclusion of low emission rates of carbon during the onset of the PETM.

### **3. Additional model results**

#### **Distribution of seafloor CaCO<sub>3</sub>**

The temporal evolution of the global mean CaCO<sub>3</sub> composition is strikingly different in the family of scenarios with contrasting sources of carbon and initial CCDs (Fig. S15). The global average sediment CaCO<sub>3</sub> composition for the pre-PETM is 18% and 45%, respectively, for the two contrasting initial conditions (Fig. S15). With bioturbation, in the shallow initial CCD case, the global average sediment CaCO<sub>3</sub> composition decreases to a minimum at ~24 kyr. In the deep initial CCD case, the global average wt. % CaCO<sub>3</sub> decreases to a minimum at ~21 kyr. Also the model results show a notable lead in time of ~3-4 kyr to reach its minimum without bioturbation in both initial CCD cases. Intense dissolution (<15% CaCO<sub>3</sub> during the height of PETM) is reproduced in the model and is mostly obvious in the case with an

organic carbon source. Bioturbation provides an additional source of  $\text{CaCO}_3$  to surface sediments during the dissolution event ( $\text{CaCO}_3$  deposited prior to the event). Thus, simulations with bioturbation exhibit a smaller magnitude of decrease in wt. %  $\text{CaCO}_3$  than those without. They also slightly lag the non-bioturbated records in time because of mixing in of younger material as sedimentation proceeds.

An overshoot of global average wt. %  $\text{CaCO}_3$  occurs during the recovery phase of the simulation, as can be mostly clearly seen in the  $C_{\text{org}}$  scenario (Fig. S15). For example, wt. % of  $\text{CaCO}_3$  at ODP Site 690<sup>10</sup>, Site 1221<sup>11</sup>, Site 1266<sup>7</sup> and Site 999 and 1001<sup>12</sup> during the recovery interval is higher than that during the pre-CIE interval (Table S4), which might be an indicator of CCD overdeepening. A CCD overdeepening is also generated in box model treatments of fossil-fuel addition<sup>13</sup>, and is the expected response to enhanced weathering following atmospheric  $\text{CO}_2$  buildup and global warming.

We evaluate the model's ability to simulate the pattern of seafloor carbonate dissolution by comparing model results for wt. %  $\text{CaCO}_3$  as a function of depth to observations from three data-rich regions: the equatorial Pacific, Walvis Ridge, and South Indian/Southern Ocean. The model results are represented by showing the wt. %  $\text{CaCO}_3$  of each grid cell at a given depth. The conventional wisdom is that in the Early Paleogene, the CCD was shallower than it is today<sup>14</sup>, which is consistent with both the “shallow CCD” and the “deep CCD” model scenarios presented here. We determined the pre-PETM CCD in central Pacific (3.35 ~ 4 km), Walvis Ridge in South Atlantic (>4 km), and South Indian/Southern Ocean (4 ~ 4.17 km ) based on the observed distribution of sedimentary  $\text{CaCO}_3$  on the seafloor (discussed below).

The observed distribution of wt. %  $\text{CaCO}_3$  shows differential dissolution intensity among the central Pacific, Walvis Ridge and Indian/Southern Ocean sites. Our interpretation of the rather sparse sedimentary record of Pacific  $\text{CaCO}_3$  variations, including ODP Site 865, Leg 198 in Shatsky Rise (ODP Sites 1208-1212) and Leg 199 (ODP Sites 1220, 1221, 1215) in Equatorial Pacific (Table S4), is that prior to the PETM, the top of the lysocline was at ~3000m and the CCD at 3350-4000m. Sites located deeper

(Sites 164, 166, 168-170, 303, 304, 307, 315, 316) exhibit hiatuses, implying that they were below the CCD<sup>14</sup>. Site 1208, whose current depth is 3346m, is highly condensed<sup>15</sup>, and the location of the PETM is poorly known. Poor nannofossil preservation indeed suggests proximity to the CCD at some time during or after deposition, but given the poor constraints, we devalue the Site 1208 data in favor of those from other nearby sites. Zeebe *et al.*<sup>16</sup> concluded that the CCD in the Pacific prior to the PETM was shallower than 3500m, within the range of our estimates.

We locate the top of the Pacific lysocline during the main phase of the PETM at ~2500m and CCD at <2900m in the Pacific, indicating only modest shoaling. In detail, in the Pacific Ocean, the wt. % CaCO<sub>3</sub> at the shallowest Site 865 (paleodepth 1300-1500m) remains essentially the same prior to (96%) and during the PETM (93%) (Table S4). At the next shallowest location (Sites 1209-1212; paleodepth 2000-3000m) exhibit high wt. % CaCO<sub>3</sub> prior to the PETM (92-98%), and only slightly lower percentages during the main phase of the PETM (78-86%) (Table S4). These features indicate that Sites 1209-1212 are located above the lysocline prior to the PETM and within the lysocline during the PETM. The wt. % CaCO<sub>3</sub> at the somewhat deeper Site 1220 (paleodepth 2900m) is about 90% prior to the PETM, decreases to <20% throughout the PETM, then increases to ~100% after the PETM. These features suggest that Site 1220 lies at or above the lysocline before the event, at or below the CCD during the event, and above the lysocline after the event. The wt. % CaCO<sub>3</sub> at deep Site 1221 (paleodepth 3200m) varies between 20% to 80% prior to the PETM, decreases to close to 0% during the peak PETM, then increases up to ~90% after the PETM. The wt. % CaCO<sub>3</sub> at similarly deep Site 1215 (paleodepth 3200m) varies between 60% to 80% prior to the PETM and decreases to ~10% during the PETM. Based on these observations, we conclude that the CCD during the PETM was shallower than or close to 2900m. Overall the CCD shoaled approximately 450 – 1100 m during the PETM in the Pacific Ocean.

In the well-studied region around Walvis Ridge in the Atlantic, there is large uncertainty in placing the lysocline and CCD prior to and during the PETM because of lack of deep sites: the top of lysocline seems

to reside at ~3200 and the CCD at >4000m, based on ODP Leg 208 (Sites 1262, 1263, 1266 and 1267), DSDP Site 527 and an earlier reconstruction of CCD in the Atlantic<sup>14, 17</sup> (Table S4). All these sites contain more than 70% CaCO<sub>3</sub> prior to the PETM even in the deepest Site 1262 (paleodepth: 3600 m)<sup>7</sup>. But during the main phase of PETM, all sites show no more than 4% CaCO<sub>3</sub>, even in the shallowest Site 1263 (paleodepth: 1500 m). Thus the CCD during the PETM was shallower than 1500 m<sup>7</sup>, but the top of the lysocline is uncertain because of lack of sites shallower than 1500 m. As a result, the CCD at Walvis Ridge shoaled more than 2000 m.

In the Southern Ocean (ODP Site 690)/the South Indian Ocean (DSDP Sites 738, 259, 248, 250 and ODP Site 752) (Table S4), the top of the lysocline prior to the PETM is uncertain, but was likely between 2 and 4 km because Site 259 (paleodepth ~4 km, paleolatitude ~55°S<sup>18</sup>) has a lower CaCO<sub>3</sub> content (61%) than shallower sites, including Sites 752 (80%; paleodepth: 1000 - 2000m), 738 (90%; paleodepth: 1350m) and 690 (84%; paleodepth: 2100m)<sup>18</sup>. Site 248 (paleodepth ~4170 m) and Site 250 (paleodepth ~5080 m) are characterized by hiatuses before and during the Paleocene-Eocene boundary. Thus, the CCD prior to the PETM in Southern Ocean/Indian Ocean was between 4000 and 4170 m. During the main phase of the PETM, all the sites in this region exhibit a decrease in CaCO<sub>3</sub> content, suggesting that they were all within a lysocline that has shoaled somewhat. Nevertheless, all sites remained above the CCD throughout the event.

To put these inferences of CaCO<sub>3</sub> response to the PETM on a more quantitative footing, and to allow for model-data comparison, we employ a statistical approach that establishes average profiles of CaCO<sub>3</sub> content as a function of depth for each region and compares observed data to these model profiles. The root mean square error (RMSE) was computed using three different depth-smoothing methods, fits to model outputs for the three regions (Fig. S5-S10), and the total RMSE was computed based on the sum of the RMSE of 3 regions. The best fit was determined by finding the smallest total RMSE.



## 4. Model-data comparison

### Methods

Three different depth-smoothing methods are applied to the model output to test the sensitivity of the RMSE comparisons to the choice of smoothing algorithm. The three methods are logistic regression (**R**), a logistic curve fit (**C**), and a logit-transformed loess fit (**L**). All of the methods use some variant of a logistic function to constrain the smoothed fits to lie between 0 and 100 wt. %.

Logistic regression (**R**) is the common statistical technique. It is implemented here as a generalized linear model in the R statistical programming language<sup>19</sup> using the ‘glm’ function, with a logit link function in the quasi-binomial family. Predictions are made using ‘predict.glm’ on the scale of the response variable. The predictions of a logistic regression asymptotically approach 100 or 0% as the depth goes to  $\pm\infty$ .

The logistic curve fit (**C**) assumes that the model  $\text{CaCO}_3$  wt. % as a function of depth ( $z$ ) follows a 4-parameter logistic function of the form

$$\text{CaCO}_3(z) = w_- - \frac{w_- - w_+}{1 + \exp[-(z - z_0)/\tau]}.$$

The parameters are  $w_+$  and  $w_-$ , the wt. % that the curve approaches as  $z \rightarrow \pm\infty$ ; a transition depth  $z_0$  where wt. % drops from high to low; and a depth range  $\tau$  over which the transition occurs. Unlike logistic regression, the logistic curve fit allows wt. % to asymptotically approach values other than 100 and 0%. A nonlinear least squares fit of this curve is performed using the R ‘nls’ function with the Port ‘nl2sol’ algorithm, constraining the values of the parameters so that  $35\% < w_+ < 100\%$ ,  $0\% < w_- < 65\%$ ,  $1000 \text{ m} < z_0 < 4000 \text{ m}$ , and  $250 \text{ m} < \tau < 1250 \text{ m}$ .

The logit loess fit (**L**) performs a logit transformation on the model output to expand the response range

[0,100] to  $[-\infty, +\infty]$ , applies nonparametric locally weighted polynomial (loess) smoothing to the transformed data, and inverts the logit transformation to put the smoothed fit on the scale 0 to 100%. Like logistic regression, the logit loess fit asymptotically approaches 0 or 100 wt. % with depth. Unlike logistic regression or the logistic curve fit, the logit loess fit is nonparametric and can adapt to local nonlinear features in the model output. The logit transformation is numerically conditioned so that very small ( $<0.1$ ) or very large ( $>99.9$ ) wt. % values are replaced by 0.1% or 99.9% before transforming. The loess fit is performed using the R function 'loess' with  $\alpha=0.9$  for the smoothing span parameter and  $\lambda=1$  for the polynomial degree parameter for all fits.

The model-data comparison methods used here differ from Panchuk *et al.*<sup>20</sup> who applied loess fits directly to both the untransformed model output and the core data. Panchuk *et al.*<sup>20</sup> used different loess parameters for different fits (whereas here we apply the same parameters to all fits). Fits to untransformed data potentially allow the fit curves to be negative or exceed 100%; the methods here use logistic transformations to enforce the appropriate bounds on the response variable. Finally, the methods here smooth only the model output, not the data, to guard against overestimating the quality of the data-model fit.

## Results

In the Pacific, which is the largest carbon reservoir among the ocean basins, and Southern Ocean, RMSE of the deep and shallow CCD initial conditions are essentially the same (Fig. S10; Table S1) when applying Logistic regression and logistic curve fit, while logit loess fit shows a slight lower RMSE for the deep CCD. However, RMSE differs markedly for Walvis Ridge, resulting in a much smaller total RMSE in the three ocean basins for the deep CCD than for the shallow CCD.

The PETM model results that we compare to the data (Fig. S6-S8; Table S2) are for the timeslice with the

maximum extent of dissolution for each run. In the case of a pre-existing shallow CCD with  $C_{org}$ , almost all the seafloor  $CaCO_3$  is dissolved no matter bioturbation is on or off (Table S2). A similarly poor model-data comparison arises for the case of a deep initial CCD and methane forcing, which dissolves very little  $CaCO_3$ . In contrast, with  $CH_4$  forcing and an initially shallow CCD, or with  $C_{org}$  and an initially deep CCD, the distribution of wt. %  $CaCO_3$  reproduces well the observations in the Pacific and Walvis Ridge and are consistent with the Southern Indian/Southern Ocean observations (Figs. S6-S8). At the acme of PETM dissolution, total RMSEs (Fig. S8) of simulations with shallow initial CCD and  $CH_4$  forcing and deep initial CCD with organic C forcing are statistically indistinguishable (Fig. S10, Table S2).

Thus, the deep CCD configuration prior to the PETM and an  $C_{org}$  source associated with a large cumulative addition (13,000 Pg C) compares most favorably to the data from an objective, statistical point of view. However, because the number of observations is quite small, we cannot definitively rule out the alternative scenario involving a smaller cumulative addition (~2200 Pg C) from biogenic methane.

## 5. Sensitivity analysis

A sensitivity analysis is carried out to evaluate the slow rate of fossil carbon emission hypothesis. We first specified the amount of  $^{13}C$ -depleted carbon emission is 50% of the total peak C input during the first 1,000 years of CIE (i.e. 1.25 Pg/yr for  $CH_4$  scenario, and 6.5 Pg/yr for  $C_{org}$  scenario), and then allowed 50% of the total peak C to be added during the following 18,000 years of CIE (i.e. 0.07 Pg/yr for  $CH_4$  scenario, and 0.36 Pg/yr for  $C_{org}$  scenario). The modeling results of the surface ocean saturation state and the  $\delta^{13}C$  responses in different reservoirs and are shown in Fig. S11 and Fig. S12 respectively.

Smooth and delay for the onset of the CIE by reworking of old sediments is demonstrated by a simple sediment mixing model as shown in Fig. S4. We assumed the duration of the CIE onset ranges from 100

years to 20,000 years; we also assumed the residence time of soil particulate carbon varies from 100 to 20,000 years.

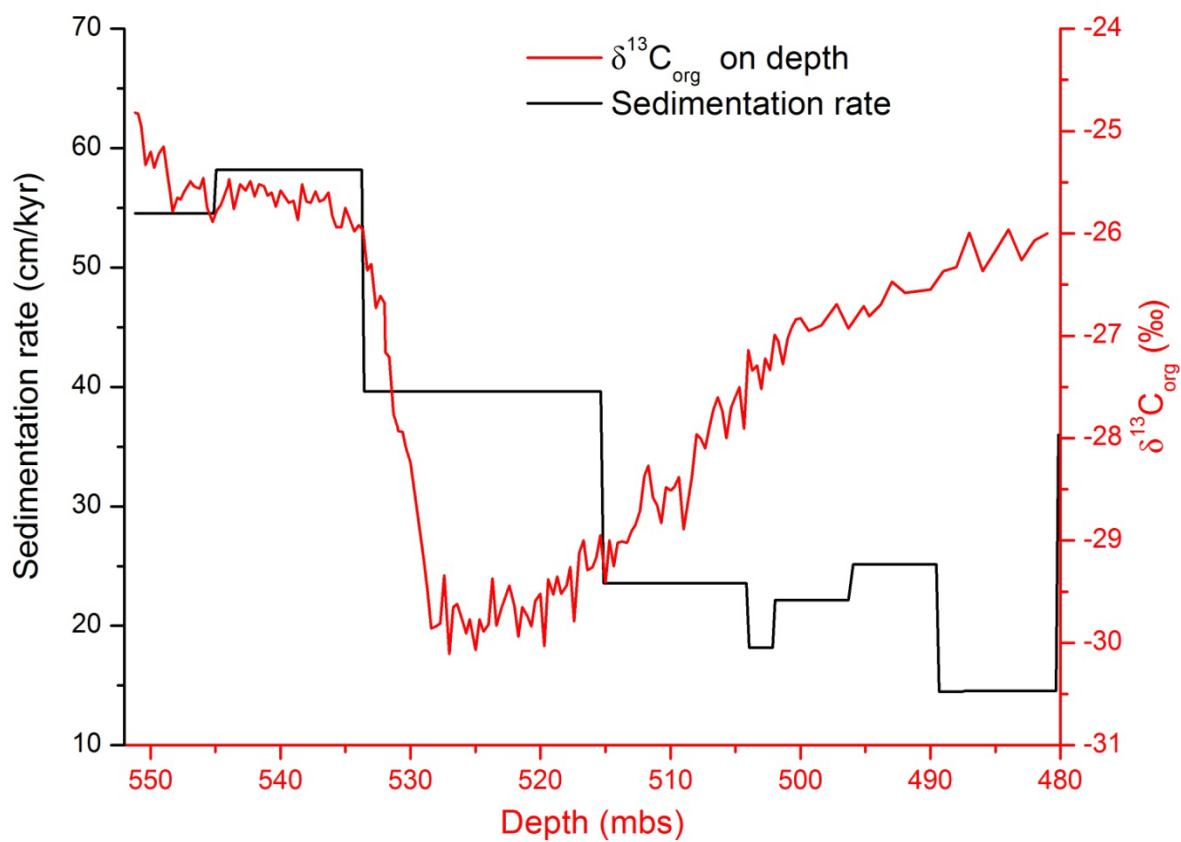


**Figure S1.** The  $\delta^{13}\text{C}_{\text{TOC}}$  and sedimentation rate from core BH9-05 in Spitsbergen plotted on depth: red solid line represents  $\delta^{13}\text{C}_{\text{TOC}}$  and the black solid line represents sedimentation rate extracted from orbital age model developed by Charles *et al.*<sup>5</sup>.

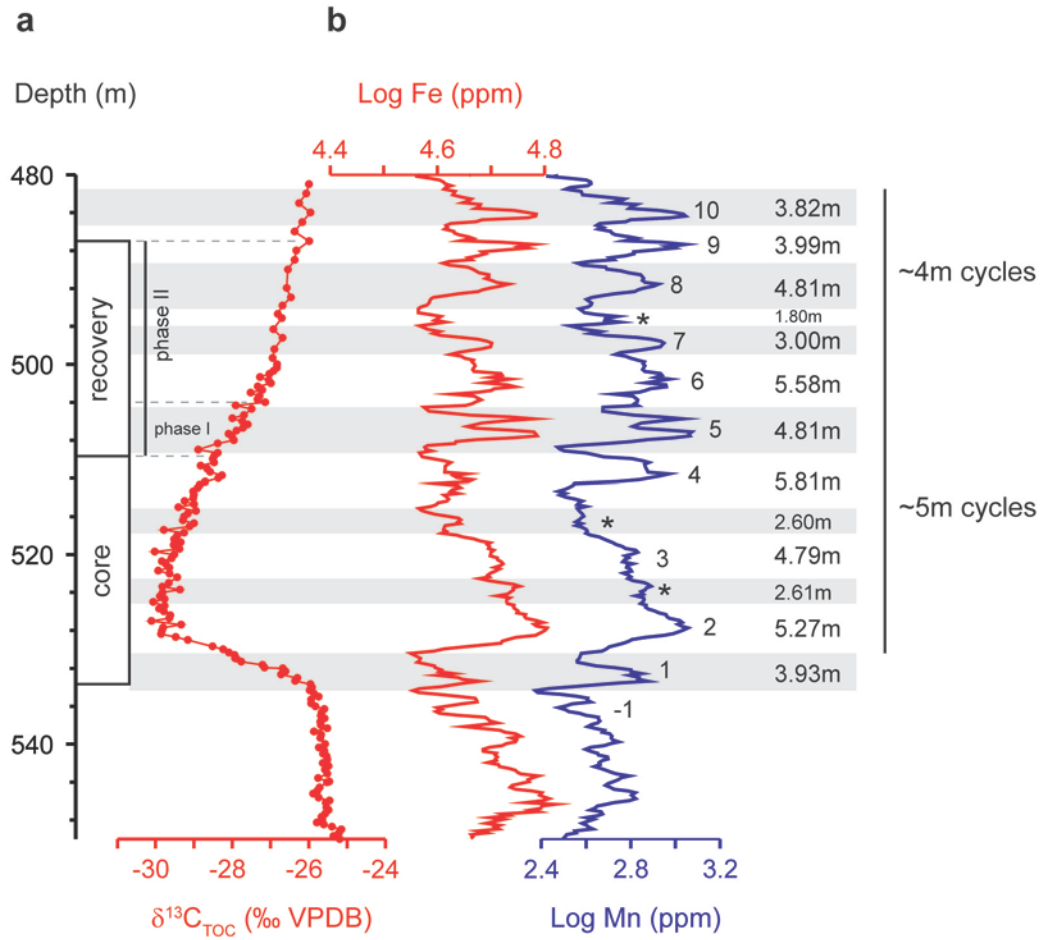


**Figure S2.** Stratigraphic thickness of inferred precession cycles during the PETM. (a)  $\delta^{13}\text{C}_{\text{TOC}}$ , showing phases of the PETM CIE as defined by Röhl *et al.*<sup>3</sup>. (b) Log Fe and Mn time-series, illustrating the stratigraphic thickness of inferred precession cycles. Cycle numbers are after Röhl *et al.*<sup>3</sup>, with potential additional precession cycles labeled with an asterisk (See Charles *et al.*<sup>5</sup> for details).

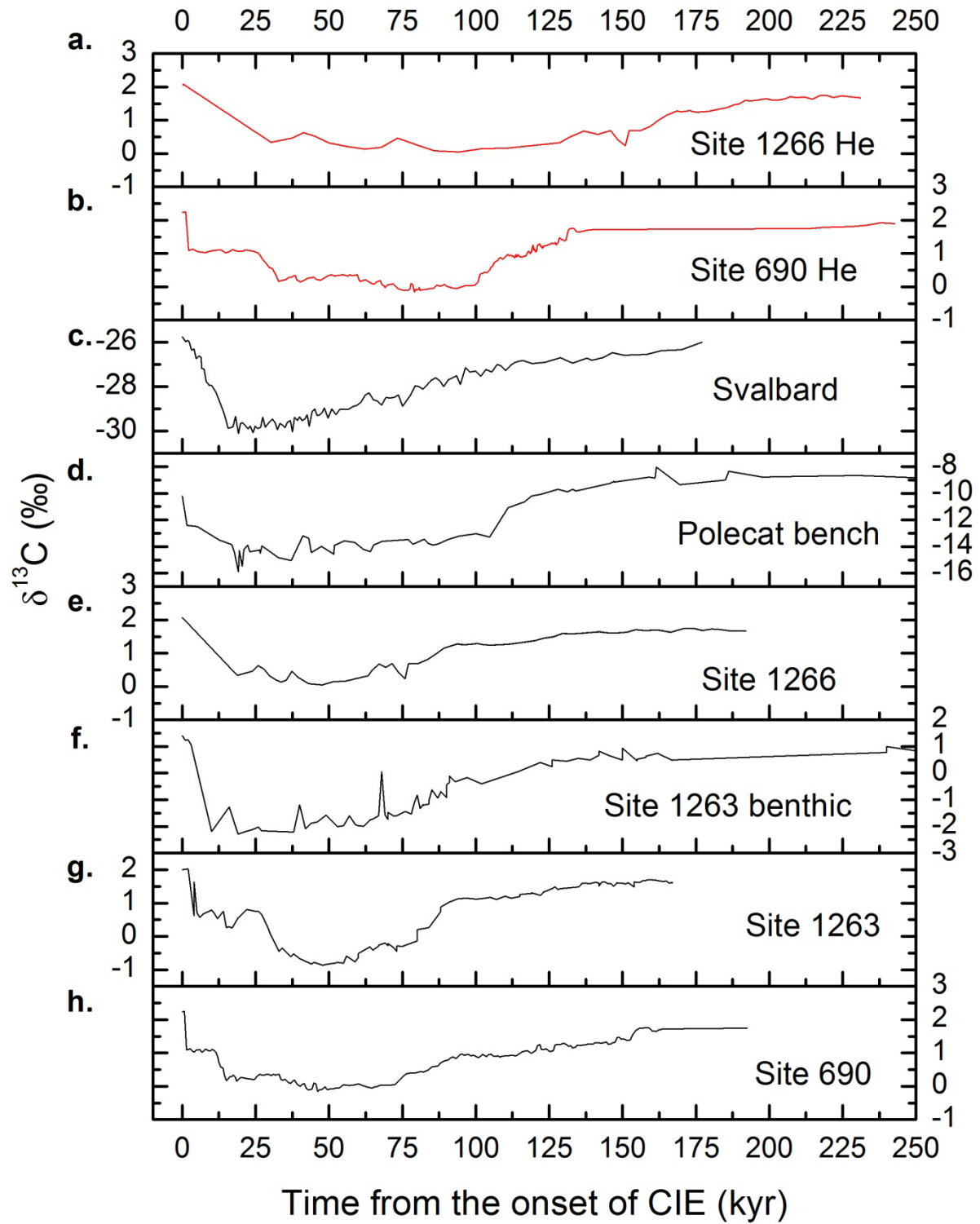


**Figure S3.** Synthesized global CIEs vs. their relative age. (a)  $\delta^{13}\text{C}$  of Site 1266 bulk carbonate on  $^3\text{He}$  time scale (from Murphy *et al.*<sup>4</sup>). (b)  $\delta^{13}\text{C}$  of Site 690 bulk carbonate on  $^3\text{He}$  time scale (from Bowen and

Zachos<sup>21</sup>). (c)  $\delta^{13}\text{C}$  of Svalbard (Spitsbergen) bulk organic C (this study), orbital age model from Charles *et al.*<sup>5</sup>. (d)  $\delta^{13}\text{C}$  of Polecat bench paleosol carbonate on orbital time scale (from Bowen and Zachos<sup>21</sup>). (e) Site 1266 on orbital time scale (from Zachos *et al.*<sup>7</sup> and Röhl *et al.*<sup>3</sup>). (f)  $\delta^{13}\text{C}$  of Site 1263 benthic foraminifera on orbital time scale (from McCarren *et al.*<sup>8</sup>). (g)  $\delta^{13}\text{C}$  of Site 1263 bulk carbonate on orbital age scale (from McCarren *et al.*<sup>8</sup>). (h) Interpolated bulk carbonate  $\delta^{13}\text{C}$  of Site 690 on orbital age scale (from Röhl *et al.*<sup>3</sup> and Bains *et al.*<sup>22</sup>).

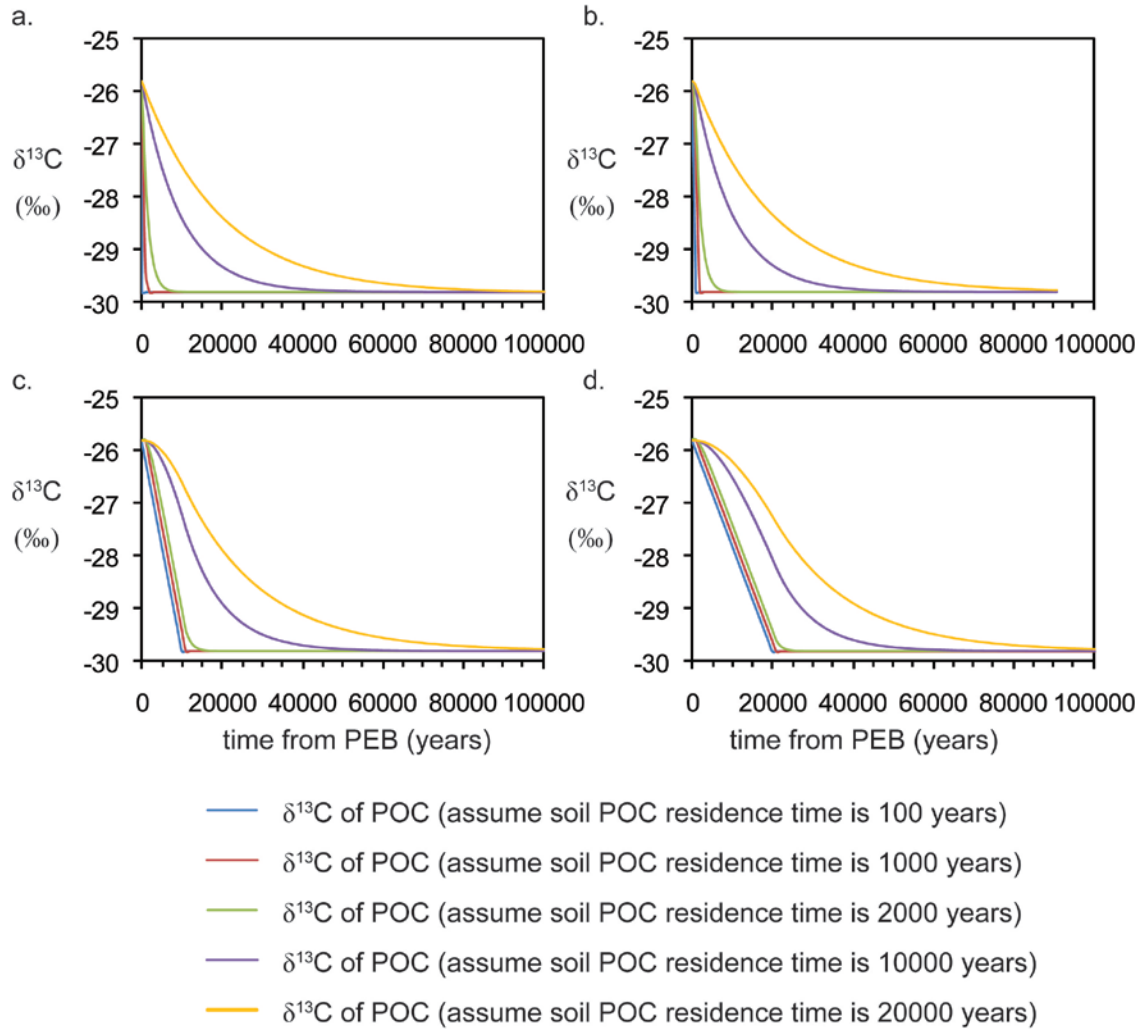


**Figure S4.** Carbon isotope records of sedimentary organic matter assuming the residence time of soil POC ranges from 100 to 20000 years. (a)  $\delta^{13}\text{C}$  of sedimentary organic matter assuming the onset of the CIE is 100 years. (b)  $\delta^{13}\text{C}$  of sedimentary organic matter assuming the onset of the CIE is 1000 years. (c)  $\delta^{13}\text{C}$  of sedimentary organic matter assuming the onset of the CIE is 10000 years. (d)  $\delta^{13}\text{C}$  of sedimentary organic matter assuming the onset of the CIE is 20000 years;



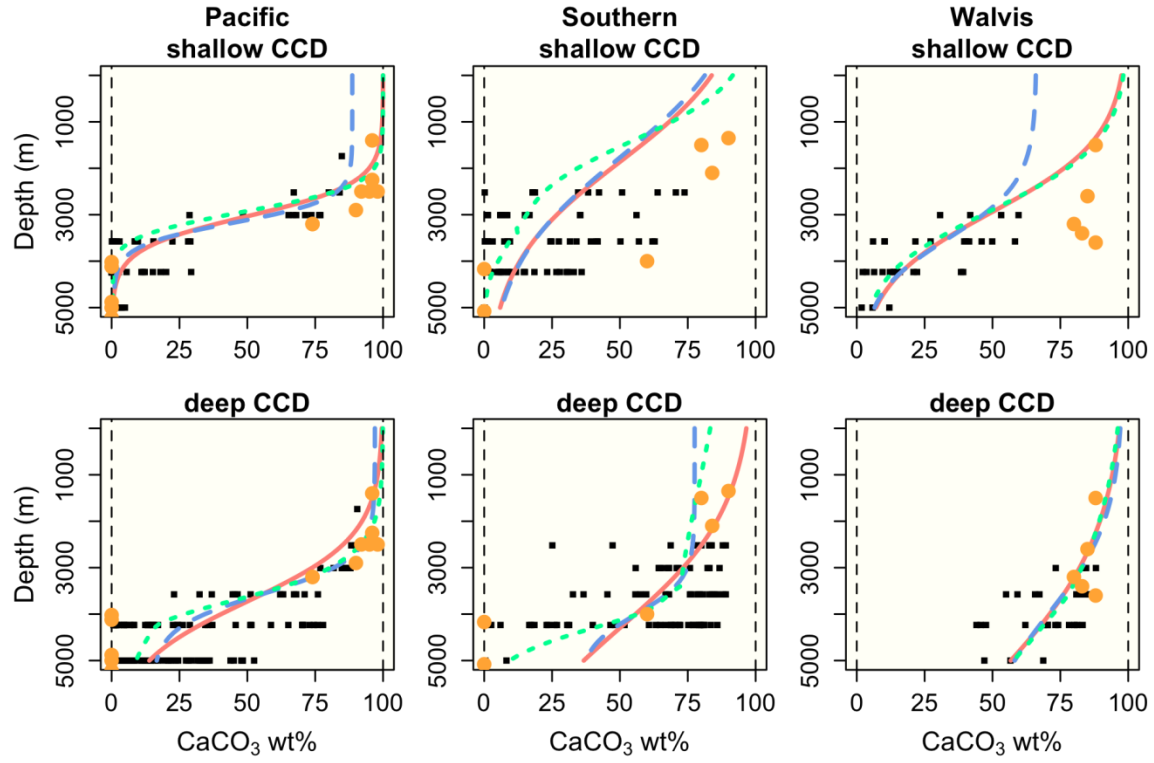


**Figure S5.** Pre-PETM model output (black squares) and output smoothed using three algorithms (**R**, red solid; **C**, blue dashed; **L**, green dotted), along with core data (orange dots) from three data-rich regions. The vertical dashed lines at 0 and 100 wt. % are guides to the eye.

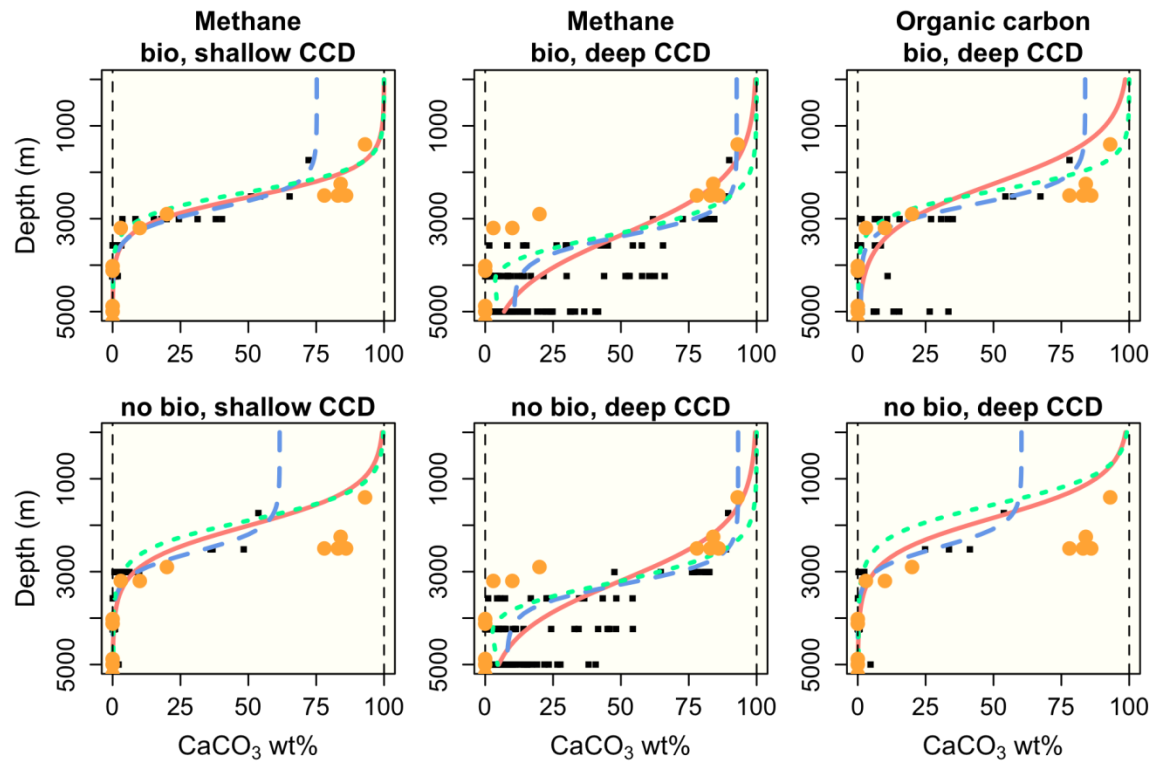


**Figure S6.** PETM central Pacific Ocean model output (black squares) and output smoothed using three algorithms (**R**, red solid; **C**, blue dashed; **L**, green dotted), along with core data (orange dots). The vertical dashed lines at 0 and 100 wt. % are guides to the eye.

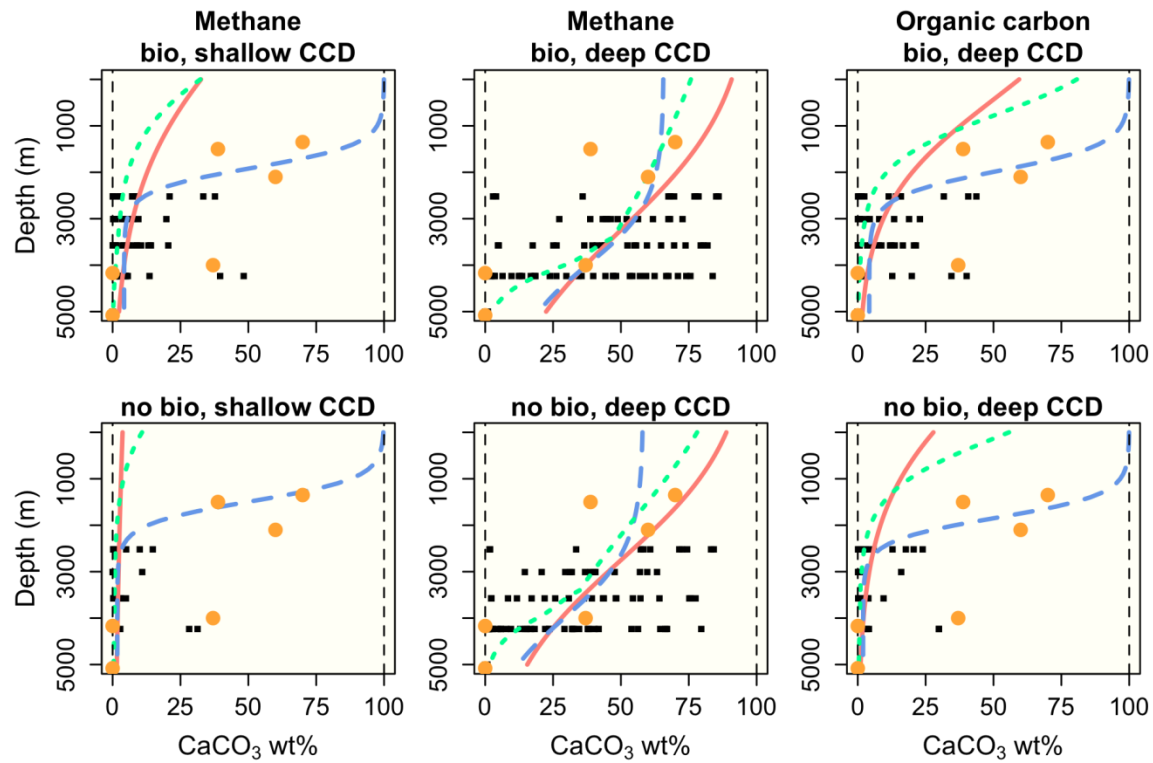


**Figure S7.** PETM Southern Ocean (Atlantic and Indian Ocean sector) model output (black squares) and output smoothed using three algorithms (**R**, red solid; **C**, blue dashed; **L**, green dotted), along with core data (orange dots). The vertical dashed lines at 0 and 100 wt. % are guides to the eye.

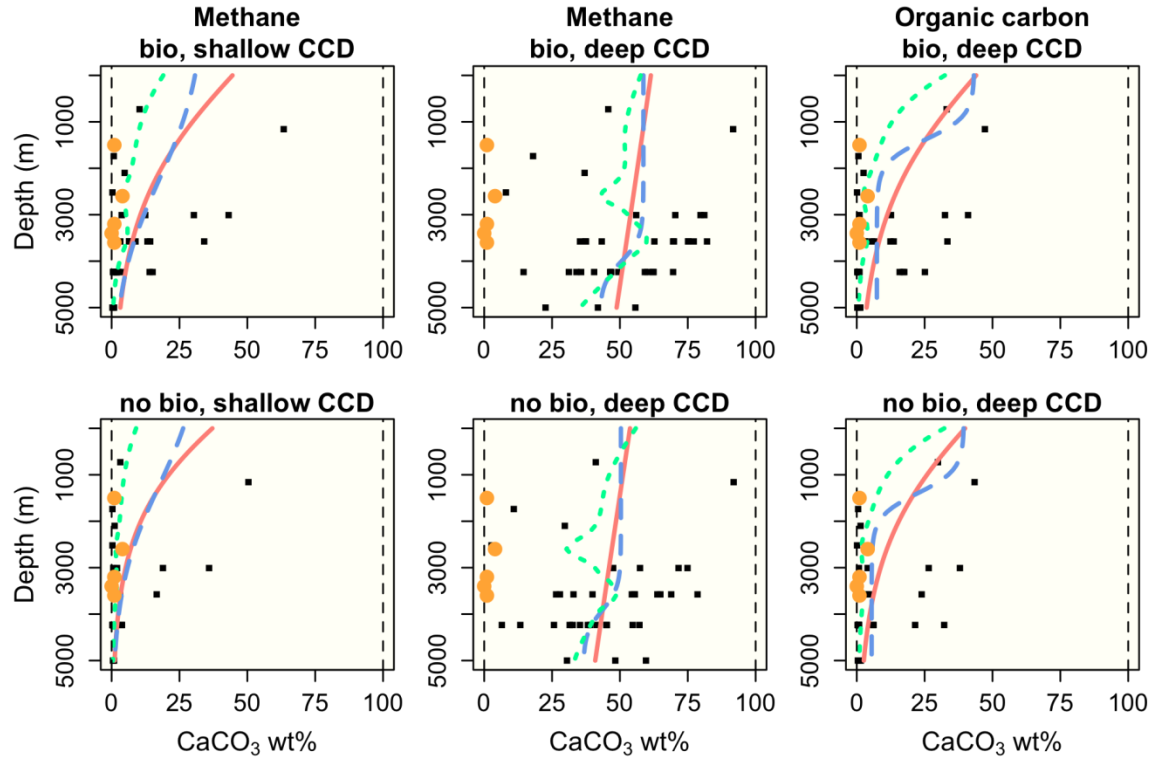


**Figure S8.** PETM Walvis Ridge in the South Atlantic Ocean model output (black squares) and output smoothed using three algorithms (**R**, red solid; **C**, blue dashed; **L**, green dotted; see text), along with core data (orange dots). The vertical dashed lines at 0 and 100 wt. % are guides to the eye.

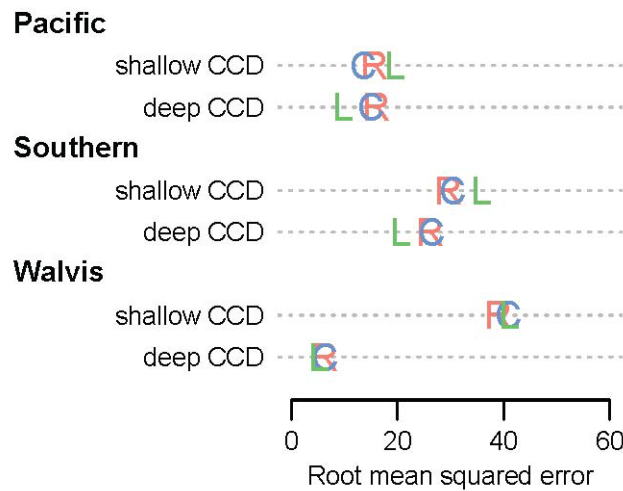


**Figure S9.** Pre-PETM root mean squared error (RMSE) between the smoothed model output and the core data, for three different smoothing algorithms (**R**, **C**, **L**; see Table S1).

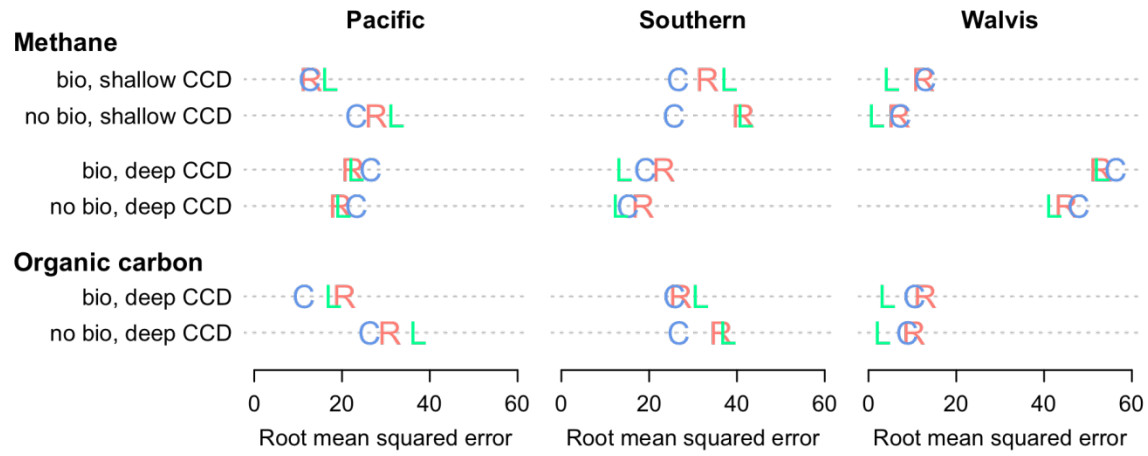


**Figure S10.** PETM root mean squared error (RMSE) between the smoothed model output and the core data, for three different smoothing algorithms (**R**, **C**, **L**; see Table S2).

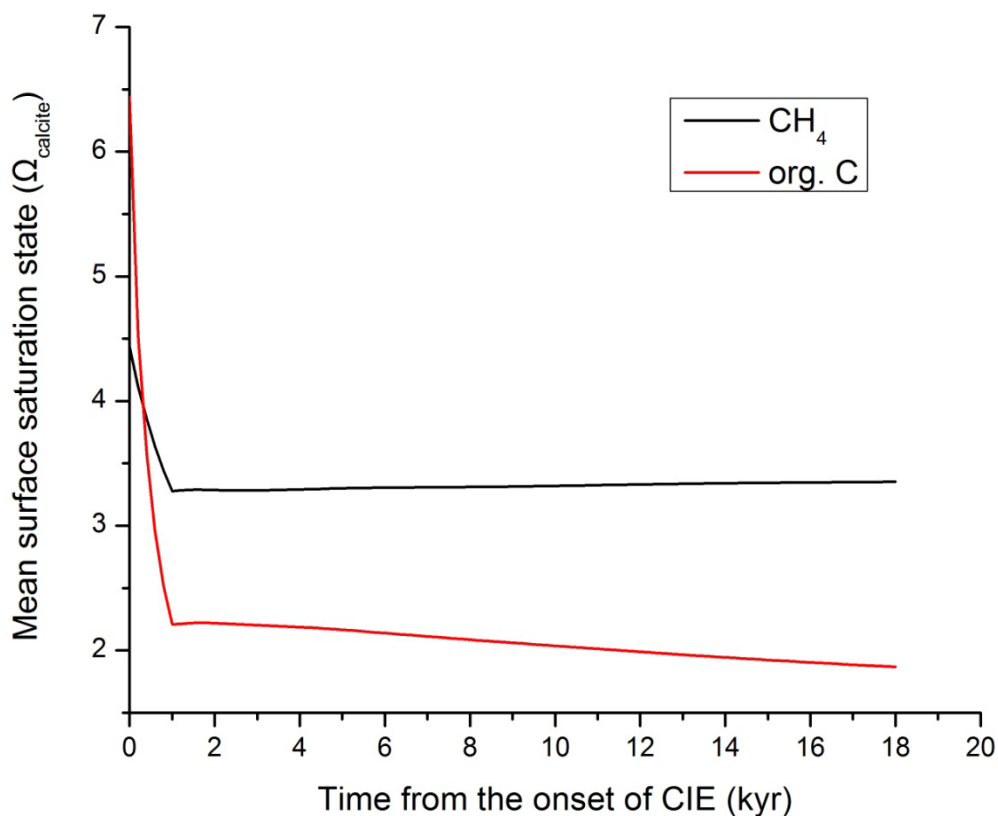


**Figure S11.** Mean surface ocean saturation state ( $\Omega_{\text{calcite}}$ ) change for both methane scenario (black line) and  $\text{C}_{\text{org}}$  scenario (red line) in sensitivity analyses. We initiated two simulations with a much more rapid pulse of carbon addition in the first 1 kyr, with half the total amount of carbon being injected, followed by 18 kyr of slow carbon injection ( $\text{CH}_4$  scenario: 1.25 Pg/yr for the first 1 kyr and 0.07 Pg/yr for the following 18 kyr;  $\text{C}_{\text{org}}$  scenario: 6.5 Pg/yr for the first 1 kyr and 0.36 Pg/yr for the following 18 kyr).

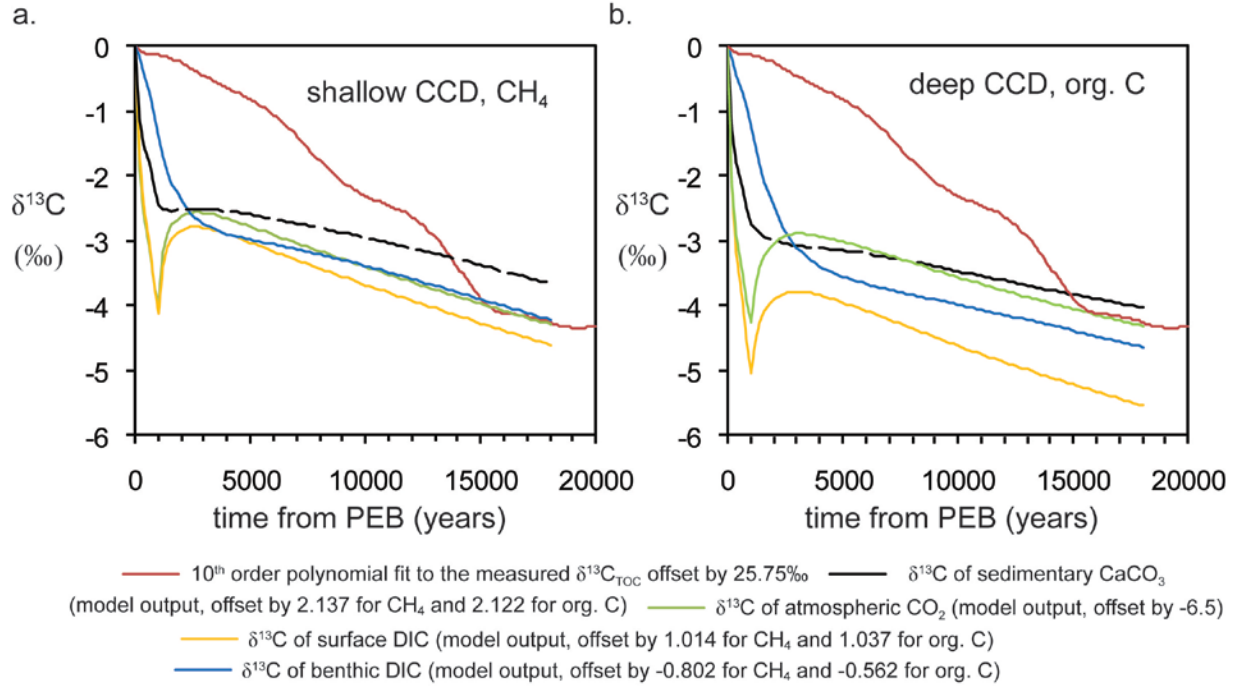


**Figure S12.** Sensitivity analysis of the  $\delta^{13}\text{C}$  response in the atmosphere, surface ocean, deep ocean and sedimentary carbonate for a faster rate of CIE onset, i.e. 50% of total C released in 1000 years, and 50% of total C released in 18000 years. (a) Modeling output in a pre-existing shallow CCD configuration with  $\text{CH}_4$  forcing, in comparison to the smoothed  $\delta^{13}\text{C}_{\text{TOC}}$  offset by 19.3‰. (b) Modeling output in a pre-existing deep CCD configuration with  $\text{C}_{\text{org}}$  forcing, in comparison to the smoothed  $\delta^{13}\text{C}_{\text{TOC}}$  offset by 19.3‰.

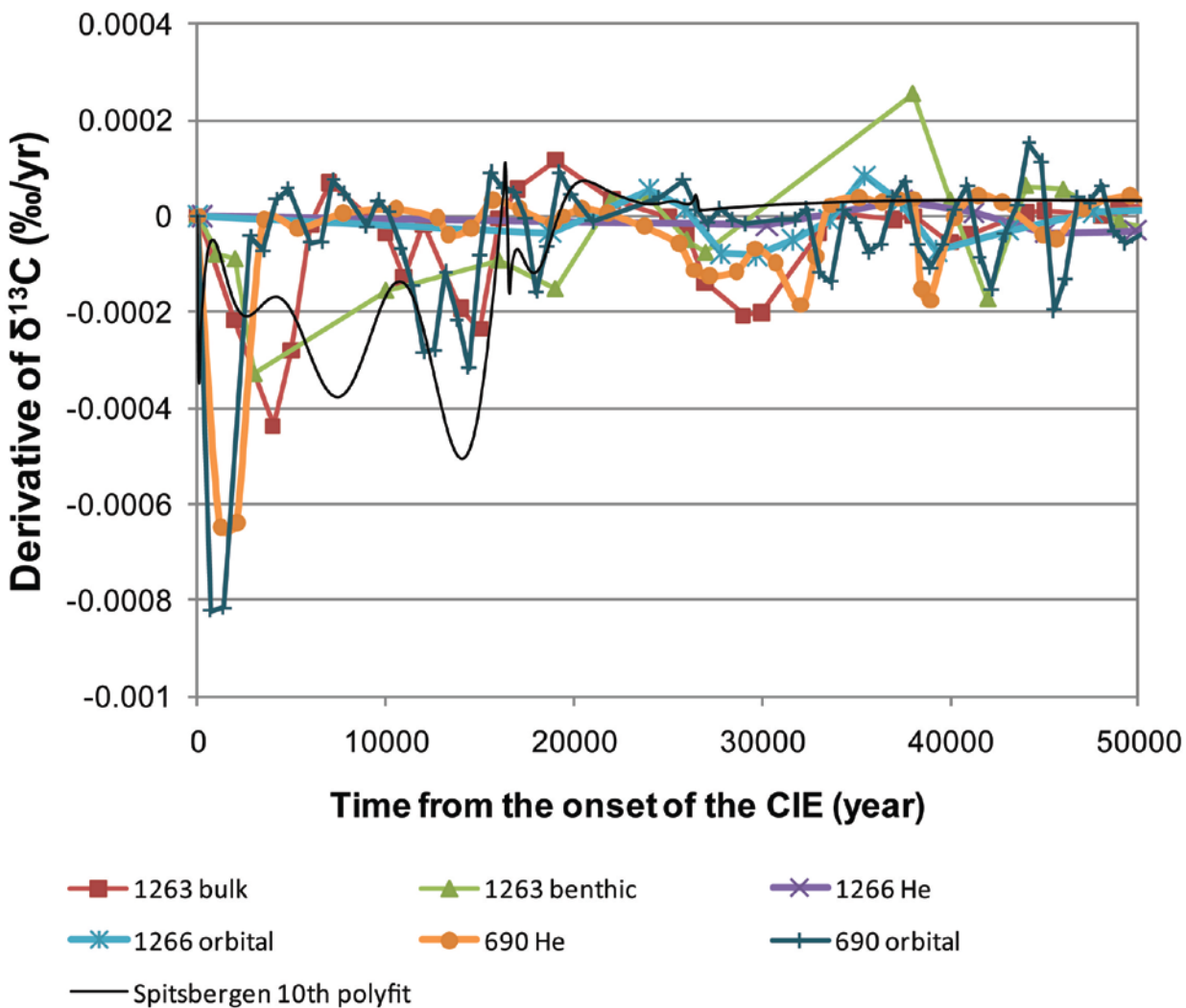


**Figure S13.** The calculated derivatives of  $\delta^{13}\text{C}$  (‰ per year) for the first 50,000 years from the onset of the CIE from Site 1263 (bulk carbonate and benthic foraminifera<sup>8</sup>), Site 1266 bulk carbonate using both  $^3\text{He}$  age model<sup>4</sup> and orbital age model<sup>3</sup>, and the 10<sup>th</sup> order polynomial fit to the  $\delta^{13}\text{C}_{\text{TOC}}$  from Spitsbergen (this study).



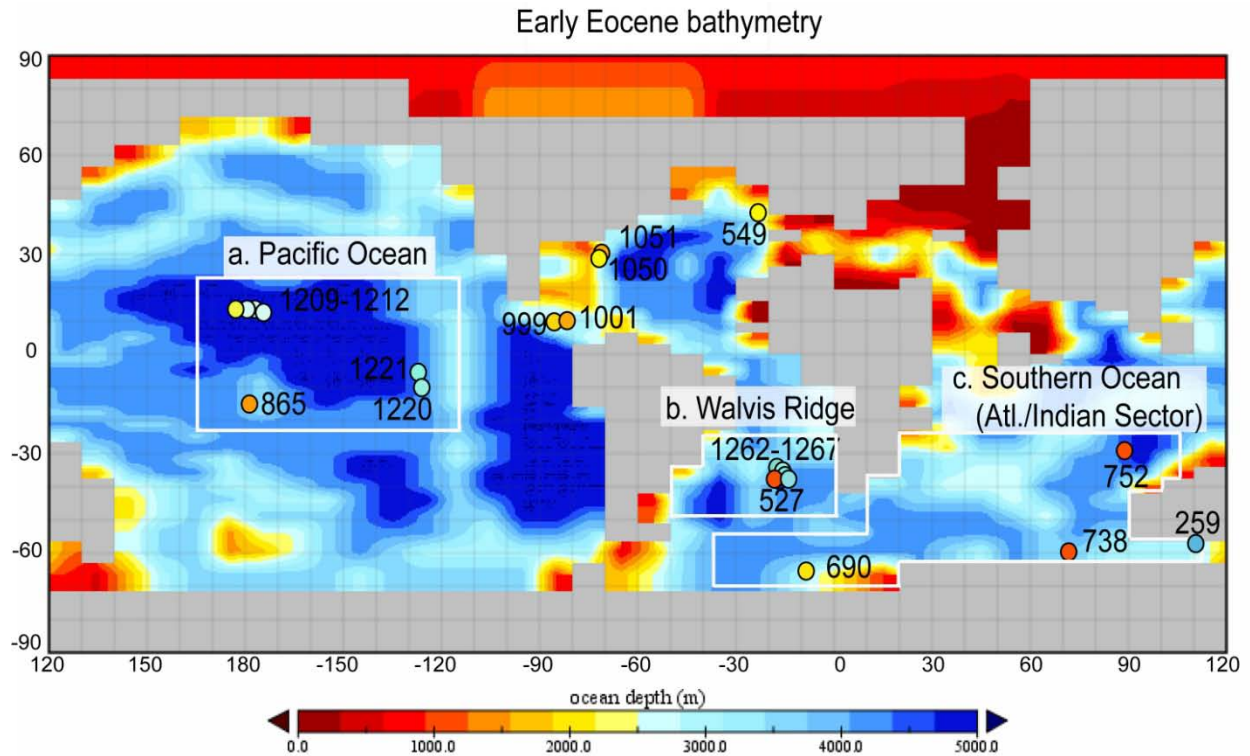


**Figure S14.** Early Eocene paleogeography and paleobathymetry in model configuration (from Bice *et al.*<sup>23</sup>). Three data-rich regions are shown in white boxes, including (a) The central Pacific Ocean. (b) Walvis Ridge in the South Atlantic Ocean. (c) Southern Ocean (Atlantic and Indian Ocean sector). Paleodepths of these sites are shown in corresponding colors. Refer to Table S4 for their paleodepths and wt. %  $\text{CaCO}_3$  values and sources.

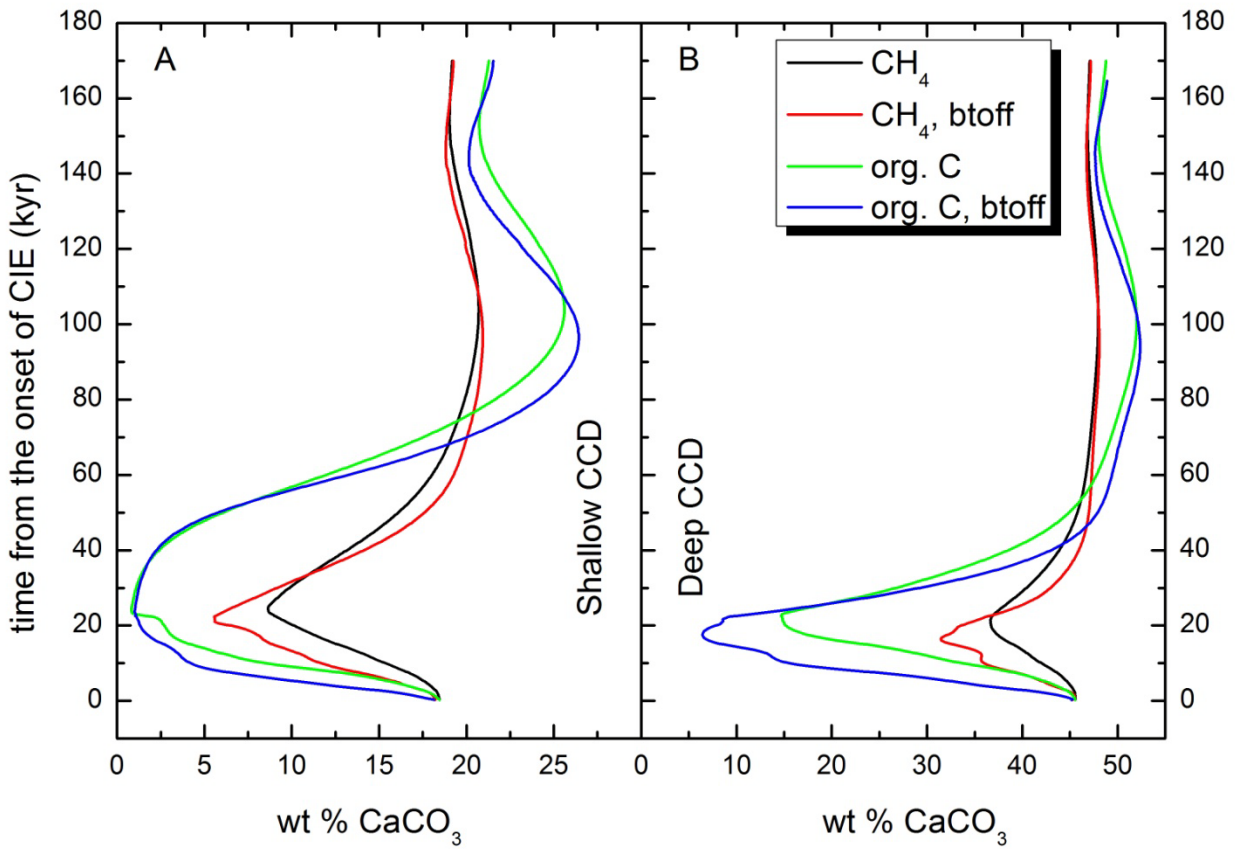


**Figure S15.** Temporal variation of global average wt. %  $\text{CaCO}_3$ . (A) an initially shallow CCD configuration; (B) an initially deep CCD configuration. Symbols are the same for (A) and (B): black solid line represents  $\text{CH}_4$  forcing, with bioturbation; red solid line represents  $\text{CH}_4$  forcing without bioturbation; green solid line represents  $\text{C}_{\text{org}}$  forcing, with bioturbation; blue solid line represents  $\text{C}_{\text{org}}$  forcing, without bioturbation.

**Table S1.** RMSE results of model-data comparison for the pre-PETM condition

Initial CCD	Ocean Basin	RMSE		
		Logistic regression (R)	Logistic curve fit (C)	Logit loess (L)
Shallow	Pacific	15.6	13.6	19.5
Shallow	Walvis Ridge	39.0	40.9	41.0
Shallow	Southern Ocean	29.5	30.5	35.8
Deep	Pacific	15.9	15.1	9.7
Deep	Walvis Ridge	6.1	6.4	5.2
Deep	Southern Ocean	26.2	26.5	20.6
Shallow	total	84.0	85.0	96.3
Deep	total	48.2	48.0	35.4

**Table S2.** RMSE results of model-data comparison for the PETM condition. Numbers in gray indicates they are not shown in Fig. S5-S7 and Fig. S9.

Initial CCD	Ocean Basin	Forcings	RMSE		
			Logistic regression (R)	Logistic curve fit (C)	Logit loess (L)
Shallow	Pacific	methane, bio	12.9	12.7	17.3
		methane, no bio	27.8	23.3	32.4
		org, bio	45.6	45.6	46.0
		org, no bio	46.1	45.4	45.8
Shallow	Walvis Ridge	methane, bio	12.5	12.9	5.3
		methane, no bio	7.0	7.3	1.9
		org, bio	1.8	4.1	1.8
		org, no bio	1.6	3.9	1.7
Shallow	Southern Ocean	methane, bio	33.2	26.6	38.2
		methane, no bio	41.5	25.7	42
		org, bio	43.4	41.0	43.4
		org, no bio	43.2	38.6	43.3
Deep	Pacific	methane, bio	22.5	26.6	23.2
		methane, no bio	19.6	23.3	20.2
		org, bio	20.6	11.3	18.1
		org, no bio	31.0	26.2	37.3
Deep	Walvis Ridge	methane, bio	52.9	56.3	53.1
		methane, no bio	45.0	48.0	42.2
		org, bio	13.0	10.5	4.3
		org, no bio	10.4	9.0	3.3
Deep	Southern Ocean	methane, bio	23.4	19.2	14.3
		methane, no bio	18.6	15.2	13.5
		org, bio	27.2	25.8	31.8
		org, no bio	36.4	26.8	38.0
Shallow	total	methane, bio	58.6	52.2	60.8
		methane, no bio	76.3	56.2	76.3
		org, bio	90.9	90.6	91.2
		org, no bio	90.9	87.8	90.7
Deep	total	methane, bio	98.8	102.1	90.6
		methane, no bio	83.2	86.4	75.9
		org, bio	60.9	47.6	54.3
		org, no bio	77.8	61.9	78.7

**Table S3.** Peak rate, cumulative amount of C addition,  $p\text{CO}_2$  and surface ocean temperature during the PETM for eight simulations

Simulation	Bioturbation	Peak Flux (Pg/yr)	Peak cumulative amount (Pg C)	Peak $p\text{CO}_2$ (ppm)	Peak Temp ( $^{\circ}\text{C}$ )
Shallow CCD, CH <sub>4</sub>	on	0.28	2504	1480	29.2
Shallow CCD, CH <sub>4</sub>	off	0.28	2503	1516	29.3
Shallow CCD, Org. C	on	1.44	11229	4431	33.9
Shallow CCD, Org. C	off	1.44	11279	4561	34.0
Deep CCD, CH <sub>4</sub>	on	0.33	3020	1428	29.0
Deep CCD, CH <sub>4</sub>	off	0.33	3022	1440	29.1
Deep CCD, Org. C	on	1.67	12894	4219	33.7
Deep CCD, Org. C	off	1.68	12974	4406	33.9

**Table S4.** wt. % CaCO<sub>3</sub> data, paleodepth, locations and sources in the central Pacific Ocean, Walvis Ridge and the southern Indian Ocean/Southern Ocean prior to and during the PETM used in this study.

Site	Latitude	Longitude	Paleodepth		Sediment CaCO <sub>3</sub> wt. %		
			Paleo depth (m)	Source	Baseline	PET M	Source
Pacific Ocean							
164	13°12.14'N	161°30.98'W	5220	Van Andel <sup>14</sup>	0(hiatus)	-	Van Andel <sup>14</sup>
166	3°45.7'N	175°4.8'W	4880	Van Andel <sup>14</sup>	0(hiatus)	-	Van Andel <sup>14</sup>
168,169	10°42.2'N	173°35.9'E	5000	Van Andel <sup>14</sup>	0(hiatus)	-	Van Andel <sup>14</sup>
170	11°48'N	177°37'E	5250	Van Andel <sup>14</sup>	0(hiatus)	-	Van Andel <sup>14</sup>
303	40°48.5'N	154°27.07'E	5540	Van Andel <sup>14</sup>	0(hiatus)	-	Van Andel <sup>14</sup>
304	39°20.27'N	155°04.19'E	5600	Van Andel <sup>14</sup>	0(hiatus)	-	Van Andel <sup>14</sup>
307	28°35.26'N	161°0.28'W	5520	Van Andel <sup>14</sup>	0(hiatus)	-	Van Andel <sup>14</sup>
315	4°10.26'N	158°31.54'W	4120	Van Andel <sup>14</sup>	0(hiatus)	-	Van Andel <sup>14</sup>
316	0°5.44'N	157°43.4'W	4020	Van Andel <sup>14</sup>	0(hiatus)	-	Van Andel <sup>14</sup>
865	18°26'N	179°33'W	1300-1500	Thomas and Shackleton <sup>24</sup>	96	93	Thomas <i>et al.</i> <sup>25</sup>
1208	36°7.6301'N	158°12.0952'W	<3346m	Colosimo <i>et al.</i> <sup>15</sup>	-	-	Colosimo <i>et al.</i> <sup>15</sup>
1209	32°39'N	158°30'E	2000-2500	Colosimo <i>et al.</i> <sup>15</sup>	96	84	Colosimo <i>et al.</i> <sup>15</sup>
1210	32°13'N	158°15'E	2000-3000	Colosimo <i>et al.</i> <sup>15</sup>	92	86	Colosimo <i>et al.</i> <sup>15</sup>
1211	32°0'N	157°50'E	2000-3000	Colosimo <i>et al.</i> <sup>15</sup>	95	70	Colosimo <i>et al.</i> <sup>15</sup>
1212	32°26'N	157°42'E	2000-3000	Colosimo <i>et al.</i> <sup>15</sup>	98	83	Colosimo <i>et al.</i> <sup>15</sup>
1215	26°01.77'N	147°55.99'W	3200	Rea and Lyle <sup>26</sup>	60-80	10	Rea and Lyle <sup>26</sup>
1220	10°10'N	142°45'W	2900	Rea and Lyle <sup>26</sup>	80-90	20	Zeebe <i>et al.</i> <sup>16</sup>
1221	12°1'N	143°41'W	3200	Rea and Lyle <sup>26</sup>	20-80	3	Murphy <i>et al.</i> <sup>11</sup>
South Atlantic							
527	28°2'S	1°45'E	3400	Moore <i>et al.</i> <sup>27</sup>	83	0	Thomas <i>et al.</i> <sup>25</sup>
1262	27°11'S	1°34'E	3600	Zachos <i>et al.</i> <sup>7</sup>	88	1	Zachos <i>et al.</i> <sup>7</sup>
1263	28°31'S	2°46'E	1500	Zachos <i>et al.</i> <sup>7</sup>	88	1	Zachos <i>et al.</i> <sup>7</sup>
1266	28°32'S	2°20'E	2600	Zachos <i>et al.</i> <sup>7</sup>	85	4	Zachos <i>et al.</i> <sup>7</sup>
1267	28°5'S	1°42'E	3200	Zachos <i>et al.</i> <sup>7</sup>	80	1	Zachos <i>et al.</i> <sup>7</sup>
North Atlantic							
1050	30°05'N	76°14'W	1000-2000	Norris <i>et al.</i> <sup>28</sup>	63	57	Rudnicki <i>et al.</i> <sup>29</sup>
549	49°05'N	13°05'W	2000-2300	Masson <i>et al.</i> <sup>30</sup>	51	1	Thomas and Bralower <sup>31</sup>

This table continues on the next page.

**Table S4.** continued

Site	Latitude	Longitude	Paleodepth		Sediment CaCO <sub>3</sub> wt. %		
			Paleo depth (m)	Source	Baseline	PETM	Source
<u>Caribbean Sea</u>							
999	12°44'N	78°44'W	1750	Thomas <i>et al.</i> <sup>25</sup>	61	0	Bralower <i>et al.</i> <sup>12</sup>
1001	15°45'N	74°54'W	1500	Thomas <i>et al.</i> <sup>25</sup>	45	0	Bralower <i>et al.</i> <sup>12</sup>
<u>Southern Ocean (Indian and Atlantic sector)</u>							
248	29°31.78'S	37°28.48'E	4170	Van Andel <sup>14</sup>	0(hiatus)	0(hiatus)	Van Andel <sup>14</sup>
250	33°27.74'S	39°22.15'E	5080	Van Andel <sup>14</sup>	0(hiatus)	0(hiatus)	Van Andel <sup>14</sup>
259	29°37'S	112°41'E	4000	Hancock <i>et al.</i> <sup>18</sup>	61	37	Hancock <i>et al.</i> <sup>18</sup>
738	62°42'S	82°47'E	1350	Barrera and Huber <sup>32</sup>	90	70	Barron and Larsen <sup>33</sup>
752	30°53.475'S	90°34.652'W	1000-2000	Barron and Larsen <sup>33</sup>	80	38.8	Barron and Larsen <sup>33</sup>
690	65°09'S	1°12'E	2100	Zachos <i>et al.</i> <sup>34</sup>	84	60	Thomas <i>et al.</i> <sup>25</sup>

**Table S5.** The measured  $\delta^{13}\text{C}_{\text{TOC}}$  (‰) from core BH9-05

Core depth (mbs)	$\delta^{13}\text{C}_{\text{TOC}}$ (‰)	Core depth (mbs)	$\delta^{13}\text{C}_{\text{TOC}}$ (‰)	Core depth (mbs)	$\delta^{13}\text{C}_{\text{TOC}}$ (‰)	Core depth (mbs)	$\delta^{13}\text{C}_{\text{TOC}}$ (‰)
481.00	-26.00	501.70	-27.05	510.35	-28.48	518.40	-29.52
482.00	-26.07	502.00	-26.99	510.70	-28.83	518.70	-29.35
483.00	-26.26	502.35	-27.34	511.00	-28.66	519.00	-29.53
484.00	-25.96	502.70	-27.22	511.35	-28.58	519.40	-29.38
485.00	-26.17	503.00	-27.52	511.70	-28.27	519.70	-30.03
486.00	-26.37	503.35	-27.29	512.00	-28.37	520.00	-29.52
487.00	-25.99	503.70	-27.34	512.35	-28.71	520.40	-29.59
488.00	-26.33	504.00	-27.14	512.70	-28.85	520.70	-29.84
489.00	-26.37	504.35	-27.91	513.00	-28.91	521.00	-29.74
490.00	-26.55	504.70	-27.50	513.35	-29.02	521.40	-29.65
491.95	-26.58	505.35	-27.70	513.70	-29.01	521.70	-29.94
492.95	-26.47	505.70	-28.00	514.05	-29.02	522.00	-29.64
493.81	-26.69	506.00	-27.74	514.35	-29.25	522.40	-29.44
494.70	-26.81	506.35	-27.60	514.70	-29.00	523.00	-29.66
495.12	-26.71	506.70	-27.72	515.00	-29.41	523.40	-29.83
496.30	-26.93	507.00	-27.89	515.40	-28.95	523.70	-29.37
497.22	-26.69	507.34	-28.10	515.70	-29.16	524.00	-29.82
498.40	-26.90	507.70	-28.00	516.00	-29.26	524.40	-29.89
499.35	-26.95	508.00	-27.96	516.40	-29.29	524.70	-29.77
500.00	-26.83	508.35	-28.38	516.70	-29.00	525.00	-30.07
500.35	-26.84	509.00	-28.89	517.03	-29.12	525.43	-29.77
500.70	-26.92	509.35	-28.38	517.40	-29.79	525.70	-29.91
501.00	-27.03	509.70	-28.48	517.70	-29.26	526.00	-29.79
501.35	-27.28	510.00	-28.51	518.00	-29.44	526.40	-29.62



**Table S5.** continued

Core depth (mbs)	$\delta^{13}\text{C}_{\text{TOC}}$ (‰)	Core depth (mbs)	$\delta^{13}\text{C}_{\text{TOC}}$ (‰)	Core depth (mbs)	$\delta^{13}\text{C}_{\text{TOC}}$ (‰)	Core depth (mbs)	$\delta^{13}\text{C}_{\text{TOC}}$ (‰)
526.72	-29.65	532.32	-26.61	538.33	-25.52	544.90	-25.78
527.00	-30.11	532.65	-26.73	538.66	-25.87	545.23	-25.89
527.40	-29.34	533.01	-26.30	539.00	-25.68	545.63	-25.75
527.72	-29.81	533.32	-26.36	539.35	-25.70	545.95	-25.46
528.05	-29.84	533.66	-25.96	540.00	-25.58	546.20	-25.56
528.40	-29.86	534.00	-25.92	540.36	-25.74	546.67	-25.54
528.70	-29.48	534.31	-25.98	540.70	-25.60	546.94	-25.49
529.00	-29.16	534.65	-25.87	541.00	-25.63	547.00	-25.51
529.70	-28.52	535.00	-25.75	541.27	-25.54	547.36	-25.58
530.00	-28.24	535.32	-25.94	541.64	-25.52	547.68	-25.67
530.35	-28.09	535.71	-25.94	542.00	-25.64	547.94	-25.65
530.60	-27.94	536.00	-25.83	542.32	-25.49	548.28	-25.79
530.94	-27.93	536.30	-25.60	542.69	-25.58	548.47	-25.61
531.00	-27.89	536.66	-25.67	543.11	-25.52	548.72	-25.40
531.30	-27.77	537.00	-25.69	543.59	-25.76	549.00	-25.15
531.63	-27.21	537.30	-25.59	543.94	-25.47	549.35	-25.22
531.94	-27.16	537.66	-25.70	544.03	-25.53	549.70	-25.36
532.00	-26.68	538.00	-25.69	544.57	-25.72		

**Table S6.** Other geochemical data

Core depth (mbs)	TOC (%) (this study)	Core depth (mbs)	Pr/Ph	Core depth (mbs)	C <sub>org</sub> /N <sub>bulk</sub>	$\delta^{15}\text{N}_{\text{bulk}}$ (‰)
501.35	1.03	483	3.85	485.19	12.3	3.681
509	1.85	493.81	4.33	493.12	12.6	3.527
510.7	0.96	500.35	4.58	497.1	12.6	3.477
527.4	1.55	504.7	5.08	504	13.1	3.443
528.05	1.88	509.35	4.04	509.19	14.7	3.204
528.4	1.68	515.4	2.51	514.08	10.5	3.247
528.7	1.50	518.7	2.16	519.01	9.7	3.492
529.7	1.40	523.7	1.56	522.14	10.9	3.572
530	1.47	525	1.46	529.27	10.9	3.575
530.35	1.26	526.4	1.46	532.48	9.5	3.385
530.35	1.39	528.05	1.44	543.5	15.1	3.483
530.6	1.32	529.7	0.95	547.45	13.9	3.55
530.94	1.33	530.35	4.07	550.06	14.0	3.427
531	1.27	531.94	4.21			
531.3	1.28	533.32	4.35			
532.65	0.98	537.3	5.52			
533.01	1.14	543.1	4.66			
533.32	1.95	544.57	4.39			
534	3.19					
534.31	2.92					
537.66	3.91					
538.33	2.77					
544.57	1.86					
544.9	1.78					
545.23	1.51					
548.47	1.82					

## References

1. Dallmann, W.K. Lithostratigraphic lexicon of Svalbard: review and recommendations for nonmenclature use: Upper Palaeozoic to Quaternary bedrock. *Tromsø, Norsk polarinstitutt*, 318 s.p. (1999).
2. Dypvik, H. *et al.* The Paleocene-Eocene thermal maximum (PETM) in Svalbard -- clay mineral and geochemical signals. *Palaeogeography, Palaeoclimatology, Palaeoecology* **302**, 156-169 (2011).
3. Röhl, U., Westerhold, T., Bralower, T.J. & Zachos, J.C. On the duration of the Paleocene-Eocene thermal maximum (PETM). *Geochemistry, Geophysics, Geosystems* **8**, Q12002 (2007).
4. Murphy, B.H., Farley, K.A. & Zachos, J.C. An extraterrestrial <sup>3</sup>He-based timescale for the Paleocene-Eocene thermal maximum (PETM) from Walvis Ridge, IODP Site 1266. *Geochimica et Cosmochimica Acta* **74**, 5098-5108 (2010).
5. Charles, A.J. *et al.* Constraints on the numerical age of the Paleocene/Eocene boundary. *Geochem. Geophys. Geosyst.* **in press**, doi: 10.1029/2010GC003426 (2011).
6. Sluijs, A., Bowen, G.J., Brinkhuis, H., Lourens, L.J. & Thomas, E. in Deep-time perspectives on climate change; marrying the signal from computer models and biological proxies. (eds. M. Williams, A.M. Haywood, F.J. Gregory & D.N. Schmidt) (Geological Society of London, London; 2007).
7. Zachos, J.C. *et al.* Rapid Acidification of the Ocean During the Paleocene-Eocene Thermal Maximum. *Science* **308**, 1611-1615 (2005).
8. McCarren, H., Thomas, E., Hasegawa, T., Röhl, U. & Zachos, J.C. Depth dependency of the Paleocene-Eocene carbon isotope excursion: Paired benthic and terrestrial biomarker records (Ocean Drilling Program Leg 208, Walvis Ridge). *Geochemistry Geophysics Geosystems* **9**, Q10008 (2008).
9. Harding, I.C. *et al.* Sea-level and salinity fluctuations during the Paleocene-Eocene thermal maximum in Arctic Spitsbergen. *Earth and Planetary Science Letters* **303**, 97-107 (2011).
10. Kelly, D.C., Zachos, J.C., Bralower, T.J. & Schellenberg, S.A. Enhanced terrestrial weathering/runoff and surface ocean carbonate production during the recovery stages of the Paleocene-Eocene thermal maximum. *Paleoceanography* **20** (2005).
11. Murphy, B.H., Lyle, M. & Lyle, A.O. Biogenic Burial across the Paleocene/Eocene Boundary: Ocean Drilling Program Leg 199 Site 1221. 1–12 (2006).
12. Bralower, T.J. *et al.* High-resolution records of the late Paleocene thermal maximum and circum-Caribbean volcanism; is there a causal link? *Geology* **25**, 963-966 (1997).
13. Walker, J. & Kasting, J. Effects of fuel and forest conservation on future levels of atmospheric carbon dioxide. *Palaeogeography, Palaeoclimatology, Palaeoecology* **97**, 151-189 (1992).
14. Van Andel, T. Mesozoic/Cenozoic calcite compensation depth and the global distribution of calcareous sediments. *Earth and Planetary Science Letters* **26**, 187-194 (1975).
15. Colosimo, A., Bralower, T. & Zachos, J. Evidence for Lysocline Shoaling at the Paleocene/Eocene Thermal Maximum on Shatsky Rise, Northwest Pacific. *Proceedings of the Ocean Drilling Program, Scientific Results* **198** (2006).
16. Zeebe, R.E., Zachos, J.C. & Dickens, G.R. Carbon dioxide forcing alone insufficient to explain Palaeocene–Eocene Thermal Maximum warming. *Nature Geoscience* **2**, 576-580 (2009).
17. Van Andel, T., Thiede, J., Sclater, J. & Hay, W. Depositional history of the South Atlantic Ocean during the last 125 million years. *The Journal of Geology* **85**, 651-698 (1977).
18. Hancock, H.J.L., Dickens, G.R., Thomas, E. & Blake, K.L. Reappraisal of early Paleogene CCD curves: foraminiferal assemblages and stable carbon isotopes across the carbonate facies of Perth Abyssal Plain. *International Journal of Earth Sciences* **96**, 925-946 (2006).
19. R Development Core Team 2010).
20. Panchuk, K., Ridgwell, A. & Kump, L.R. Sedimentary response to Paleocene-Eocene Thermal Maximum carbon release: A model-data comparison. *Geology* **36**, 315-318 (2008).

21. Bowen, G.J. & Zachos, J.C. Rapid carbon sequestration at the termination of the Palaeocene-Eocene Thermal Maximum. *Nature Geoscience* **3**, 866-869 (2010).
22. Bains, S., Corfield, R.M. & Norris, R.D. Mechanisms of climate warming at the end of the Paleocene. *Science* **285**, 724-727 (1999).
23. Bice, K.L., Barron, E.J. & Peterson, W.H. in Tectonic boundary conditions for climate reconstructions. (eds. T. Crowley & K. Burke) 227-247 (New York, Oxford University Press, 1998).
24. Thomas, E. & Shackleton, N.J. The Paleocene-Eocene benthic foraminiferal extinction and stable isotope anomalies. *Geological Society Special Publications* **101**, 401-441 (1996).
25. Thomas, D.J., Bralower, T.J. & Zachos, J.C. New evidence for subtropical warming during the late Paleocene thermal maximum: Stable isotopes from Deep Sea Drilling Project Site 527, Walvis Ridge. *Paleoceanography* **14**, 561-570 (1999).
26. Rea, D.K. & Lyle, A.O. Paleogene calcite compensation depth in the eastern subtropical Pacific: Answers and questions. *Paleoceanography* **20**, PA1012 (2005).
27. Moore Jr, T., Rabinowitz, P., Borella, P., Shackleton, N. & Boersma, A. History of the Walvis Ridge. *Initial Reports of the Deep Sea Drilling Project* **74**, 873-894 (1984).
28. Norris, R.D., Kroon, D., Klaus, A. & al., e. Proceedings of the Ocean Drilling Program, Initial Reports, Vol. 171B. *Shipboard Scientific Party*, 171-240 (1998).
29. Rudnicki, M., Wilson, P. & Anderson, W. Numerical models of diagenesis, sediment properties, and pore fluid chemistry on a paleoceanographic transect: Blake Nose, Ocean Drilling Program Leg 171B. *Paleoceanography* **16**, 563-575 (2001).
30. Masson, D., Montadert, L. & Scrutton, R. Regional geology of the Goban Spur continental margin. *Init. Rep. Deep Sea Drill. Proj* **80**, 1115-1139 (1985).
31. Thomas, D.J. & Bralower, T.J. Sedimentary trace element constraints on the role of North Atlantic Igneous Province volcanism in late Paleocene-early Eocene environmental change. *Marine Geology* **217**, 233-254 (2005).
32. Barrera, E. & Huber, B., Vol. 119 693-717 (1991).
33. Barron, J. & Larsen, B. Mineralogy and geochemistry of a basalt from Site 738: Implications for the tectonic history of the southernmost part of the Kerguelen Plateau. (1989).
34. Zachos, J.C. *et al.* A Transient Rise in Tropical Sea Surface Temperature During the Paleocene-Eocene Thermal Maximum. *Science* **302**, 1551-1554 (2003).